The Japan Society of Applied Physics

REGULAR PAPER

Transmission conditions for clear depiction of thoracic spine based on difference between reflection and scattering characteristics of medical ultrasound

Transmission conditions for clear depiction of thoracic spine based on difference between reflection and scattering characteristics of medical ultrasound

Taiga Bando[1], Shohei Mori[2], Mototaka Arakawa[1,2*], Eiko Onishi[3], Masanori Yamauchi[3], and Hiroshi Kanai[1,2]

[1]Graduate School of Biomedical Engineering, Tohoku University, Sendai 980-8579, Japan
[2]Graduate School of Engineering, Tohoku University, Sendai 980-8579, Japan
[3]Department of Anesthesiology and Perioperative Medicine, Tohoku University School of Medicine, Sendai 980-8575, Japan

*E-mail: arakawa@ecei.tohoku.ac.jp

In epidural anesthesia, it is difficult to specify the puncture position of the anesthesia needle. We have proposed an ultrasonic method to depict the thoracic spine using the different characteristics of reflection from bone and scattering from muscle tissue. In the present paper, we investigated the transmission aperture's width of the ultrasound probe to emphasize the differences in the reflection and scattering characteristics. First, we determined the optimum transmission aperture's width using a simulation experiment. Next, we measured reflection and scattering signals by changing the transmission aperture's width in a water tank experiment and confirmed that the results corresponded to the simulations. However, as the transmission aperture's width increased, the lateral resolution at the focal point improved. Therefore, better imaging of the human thoracic vertebrae can be achieved by selecting the transmission aperture's width, which considers the effect on lateral resolution.

© 2022 The Japan Society of Applied Physics

1. Introduction

Epidural anesthesia is a local anesthesia method used before surgery, and it is often combined with general anesthesia because it reduces the burden on patients intraoperatively and postoperatively.[1] The anesthesia needle is punctured from the surface of the skin into the spinal space. In epidural anesthesia for the thoracic spine, it is not easy to puncture the anesthesia needle into the proper position because the spinal space is narrow and complex. As the location of the puncture is determined by the physician's palpation at present, the success of anesthesia is dependent on the skills of the physician. The success rate of epidural anesthesia ranges from 75% to 94%,[2–4] and its failure may induce headaches and complications. During epidural anesthesia, patients reported back pain and psychological distress in 22% and 14% of the cases, respectively.[5]

Medical ultrasound confirms the puncture position before anesthesia as an aid of palpation in clinical practice.[6] In epidural anesthesia for the lumbar spine and other regional anesthesia, ultrasound guidance is often used, and its usefulness has been demonstrated.[7–10] However, it is difficult to depict clear images of the puncture position, especially for obese patients with a deep spine or thoracic vertebrae with a narrow gap.[11–13] Several studies have been proposed for the ultrasound guidance of epidural anesthesia, e.g. automatic identification of the spine.[14–16] However, these studies targeted the lumbar spine, which has a wide gap and simple structure.

Ultrasound imaging of bone is studied in the field of orthopedics.[17–20] Several methods have been proposed, e.g. using strain under pressure to identify the bone shape,[21,22] phase symmetry,[23] and shadow peaks.[24] However, it is difficult to apply these methods to the thoracic spine because it is located deep beneath the skin surface and has a complex surface structure.

We have developed an imaging method that can be applied to assist epidural anesthesia in the thoracic spine. In our previous study, we proposed three methods. The first method improves the delayed addition misalignment caused by the reflection of ultrasound at the thoracic vertebral surface,[25] and it depicts a smooth and tilted object by not

considering the transmitting and receiving positions as the same, applying the envelope method[26] and range point migration method.[27,28] The second method is based on the difference in ultrasound characteristics between soft tissue and bone,[29] which calculates the ratio of the delayed addition with a wide range along the time direction to the normal one and multiplies it by the brightness value at each point of the image. The third method is based on the difference between the reflection and scattering ultrasound characteristics.[30] This method uses angular amplitude characteristics, which are enveloped amplitudes of signals received by many elements of the ultrasonic probe at the time corresponding to the depth of the target. This method estimates whether the target is a reflector or scatterer by fitting angular amplitude characteristics obtained from the target with the reference data of reflection and scattering characteristics. The difference in the angular amplitude characteristics between reflection and scattering affects the estimation accuracy of the target.

The purpose of the present paper is to investigate the ultrasound transmission condition so that the difference in angular amplitude characteristics between reflection and scattering is more emphasized in the third method. We fundamentally investigated the difference among angular amplitude characteristics and the difference in the width of the transmission aperture.[31] Focusing on the transmission aperture, the effect of the aperture on the angular amplitude characteristics of scattering and reflection was examined by simulation. Based on the results, a better transmission aperture is determined by the simulation. Finally, simulation results were confirmed using water tank experiments.

2. Principle

2.1. Difference of angular amplitude characteristics between scattering and reflection

Figure 1 shows a wave scattered from a point scatterer when a focused wave is transmitted with a linear probe, where d and x_m are the depth of the point scatterer and the lateral position of the mth received element, respectively, $x_m = 0$ shows the center of the probe aperture, and c is the speed of sound in the medium. The time ranging from transmission at
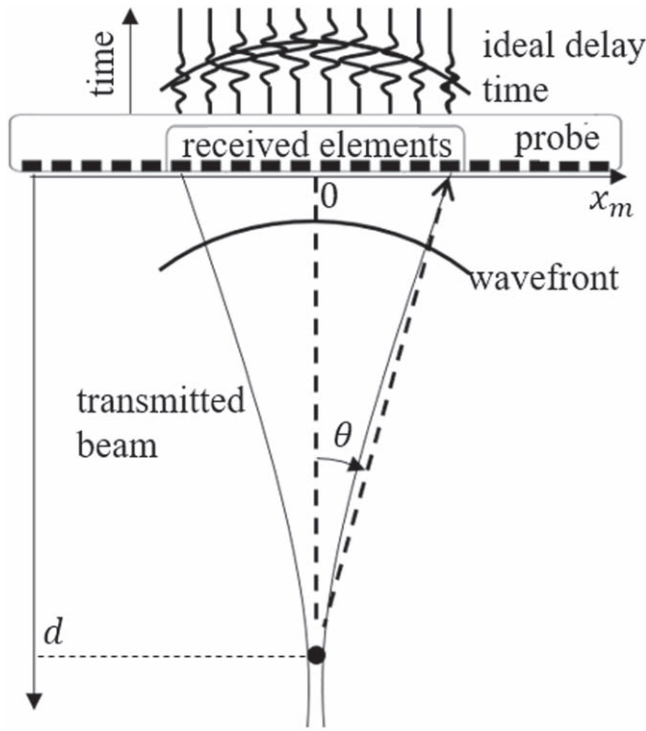
Fig. 1. Transmission and reception of a focused wave by a linear array probe.
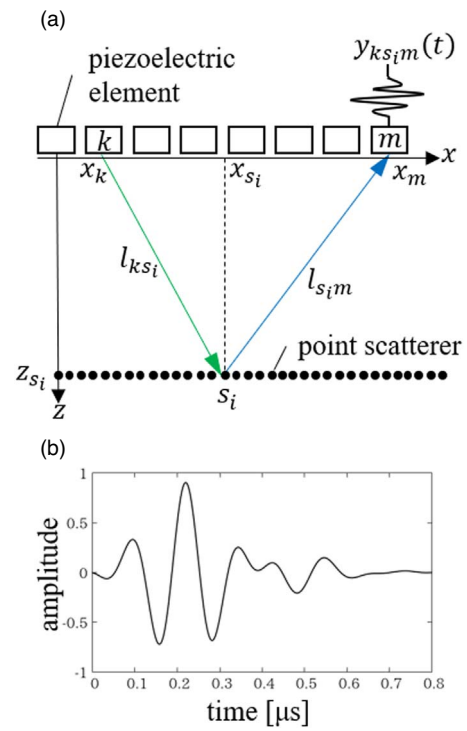

Fig. 2. (Color online) Simulation of the received signal. (a) Calculation of $y_{ks_im}(t)$. (b) Received waveform transmitted by one element, $y_0(t)$.

the center element to the receipt of the wave scattered from the point scatterer at the mth received element, $\tau_{m,d}$, is given by

$$\tau_{m,d} = \frac{d + \sqrt{d^2 + x_m^2}}{c}. \tag{1}$$

By defining the ideal delay time by $\{\tau_{m,d}\}$ and the received signal at mth element by $y_m(t)$, the angular amplitude characteristic $R(m; d)$, which shows the head amplitude of the $y_m(t)$ just at the ideal delay time $\tau_{m,d}$, is provided by the enveloped amplitude $y'_m(t)$ of $y_m(\tau_{m,d})$ as

$$R(m; d) = y'_m(\tau_{m,d}). \tag{2}$$

When an ultrasound is irradiated to a scatterer such as muscle tissue, the ultrasound is scattered along with all the directions from the object, which follows Rayleigh scattering when the scatterer is sufficiently smaller than the wavelength of the ultrasound and the angular amplitude characteristic $R_S(m; d)$ for the scattering becomes a gentle parabola.[30] On the other hand, when ultrasound is irradiated to a reflector with a regional plate, such as a bone, the ultrasound is specularly reflected, and $R_R(m; d)$ for the reflection becomes high for the direction corresponding to the specular reflection and low for other directions.[30]

2.2. Evaluation method for differences in angular amplitude characteristics

The difference between $R_R(m; d)$ and $R_S(m; d)$ was quantitatively evaluated using following the root mean square error (RMSE):

$$RMSE\,[\%] = \sqrt{\frac{\sum_m \{R_R(m; d) - \hat{A}R_S(m; d)\}^2}{\sum_m R_R(m; d)^2}} \times 100, \tag{3}$$

$$\hat{A} = \frac{\sum_m R_R(m; d)R_S(m; d)}{\sum_m \{R_S(m; d)\}^2}, \tag{4}$$

where $\hat{A}$ is the parameter that minimizes the RMSE. From $\partial RMSE/\partial A = 0$, we can determine $\hat{A}$. In the present paper, a suitable transmission aperture was determined so that the $RMSE$ becomes maximum for various transmission aperture widths.

2.3. Simulation method

Figure 2(a) shows the simulation done in this paper. The number of received elements was 96, and the element pitch was 0.2 mm, assuming the typical ultrasound diagnostic equipment with the linear probe. When the short axis of a molybdenum wire with a diameter of 30 μm was set in a water tank, the transmitted and received waveform using one element above the wire was measured using ultrasound diagnostic equipment at a center frequency of 7.5 MHz. The waveform sampled at 40 MHz was interpolated 50 times using the sinc function, and the resultant $y_0(t)$ is shown in Fig. 2(b).

The received signals from a reflector or scatterer were generated when a focused wave with a focal depth of 30 mm was transmitted. In Fig. 2(a), $y_{ks_im}(t)$, which is transmitted from the kth transmitted element, scattered by ith point scatterer s_i, and received by mth received element, is given by

$$y_{ks_im}(t) = S(k, x_{s_i}, z_{s_i}, m)\, y_0(t - \tau_{ks_im}), \tag{5}$$

where $S(k, x_{s_i}, z_{s_i}, m)$ shows theoretical scattering characteristics,

$$
\begin{aligned}
&S(k, x_{s_i}, z_{s_i}, m) \\
&= A\,(k, x_{s_i}, z_{s_i}, m)s(k, x_{s_i}, z_{s_i}, m) \\
&\quad D(x_{s_i}, z_{s_i}, m)E(x_{s_i}, z_{s_i}, m),
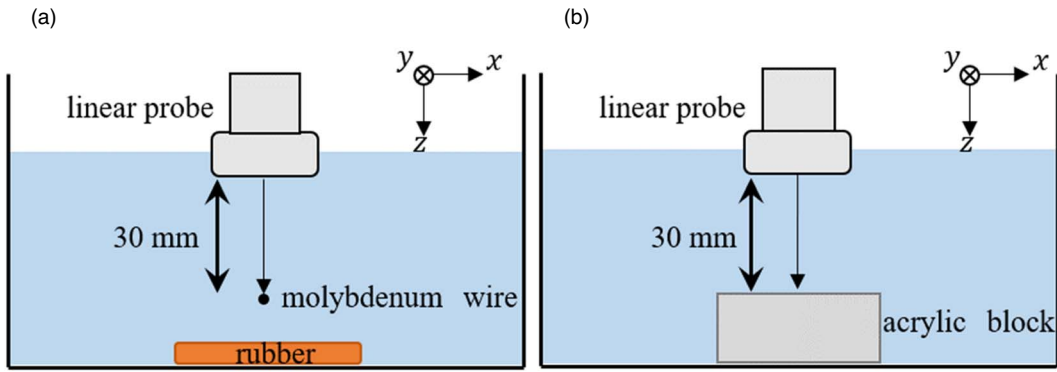\end{aligned} \tag{6}
$$

Fig. 3. (Color online) Water tank experimental system. (a) The measurement of the scattering characteristics. The short axis of a molybdenum wire with a diameter of 30 mm was measured as a scatterer. (b) The measurement of the reflection characteristics. The surface of an acrylic block was measured as a reflector.
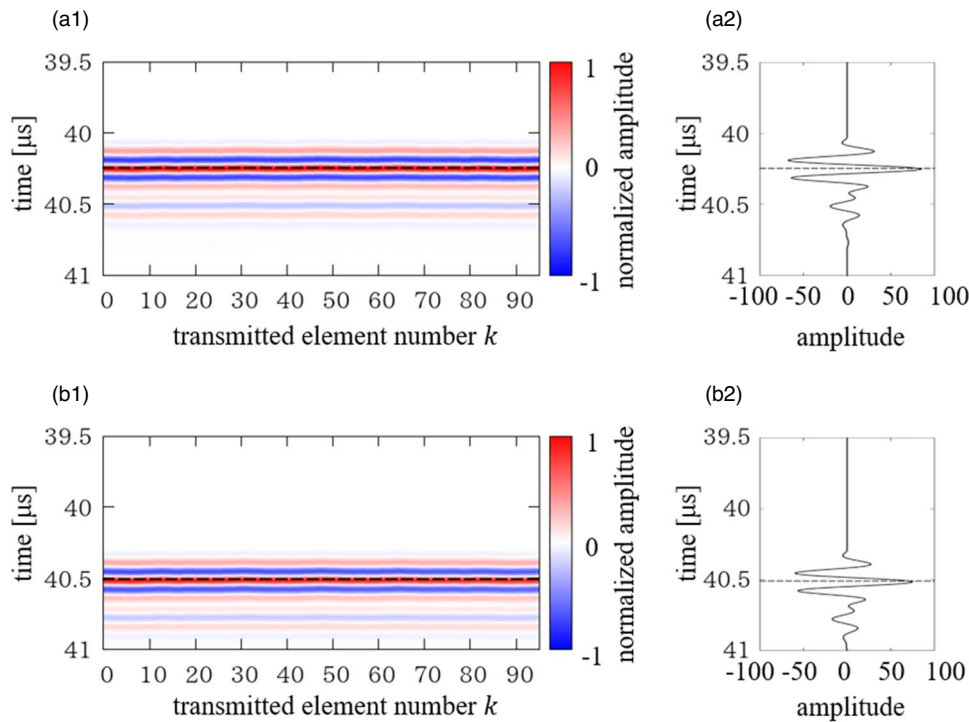

Fig. 4. (Color online) Simulation results of the scatterer. (a1), (b1) Received signals $y_{km}(t)$ from each transmitted element. (a2), (b2) Received signals $y_m(t)$; (a1), (a2) results for $x = 0$ mm; and (b1), (b2) results for $x = -4.8$ mm.

and τ_{ks_im} shows the delay time of propagation from the kth transmitted element, ith point scatterer s_i, and mth received element as

$$\tau_{ks_im} = \frac{l_{ks_i}}{c_w} + \frac{l_{s_im}}{c_w} + \tau_k, \tag{7}$$

where c_w is the speed of sound in the medium, l_{ks_i} and l_{s_im} are the path lengths from the kth transmitting element to s_i and from s_i to mth receiving element, respectively, and τ_k is the delay time of the kth element to transmit the focused wave. $S(k, x_{s_i}, z_{s_i}, m)$ of Eq. (6) comprises the propagation attenuation $A(k, x_{s_i}, z_{s_i}, m)$, the angular characteristic of Rayleigh scattering $s(k, x_{s_i}, z_{s_i}, m)$, the reception directivity of piezoelectric elements $D(x_{s_i}, z_{s_i}, m)$, and the effect of interference in the width of the piezoelectric element at the reception of ultrasound, $E(x_{s_i}, z_{s_i}, m)^{32)}$, $A(k, x_{s_i}, z_{s_i}, m)$, $s(k, x_{s_i}, z_{s_i}, m)$, and $D(x_{s_i}, z_{s_i}, m)$ are shown in Eqs. (8)–(10), respectively.

$$A(k, x_{s_i}, z_{s_i}, m) = 10^{-\alpha\,(l_{ks_i}+l_{s_im})f_0^2/20}, \tag{8}$$

$$s(k, x_{s_i}, z_{s_i}, m) \propto \frac{1 + \cos^2 \theta_{ks_im}}{2}, \tag{9}$$

$$D(x_{s_i}, z_{s_i}, m) = \cos^2 \theta_{mML}, \tag{10}$$

where α is the attenuation coefficient of water ($\alpha = 1.94 \times 10^{-4}$ dB MHz^{-2} mm^{-1})$^{33)}$; $f_0 = 7.5$ MHz, which is the center frequency of the probe used in the water tank experiments; θ_{ks_im} is the scattering angle and is defined as

$$\theta_{ks_im} = \tan^{-1}\frac{x_{s_i} - x_k}{z_{s_i}} + \tan^{-1}\frac{x_m - x_{s_i}}{z_{s_i}}, \tag{11}$$

and θ_{mML} is the incidence angle from the acoustic matching layer to the piezoelectric element given by
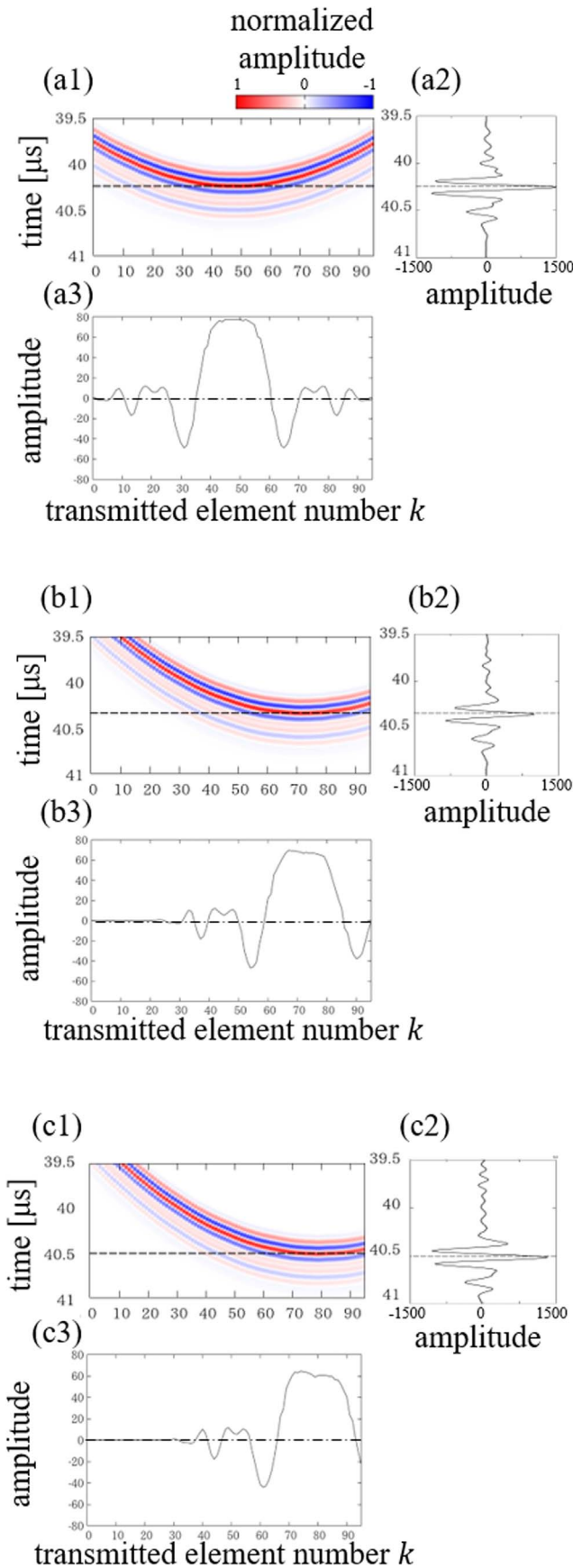
Fig. 5. (Color online) Simulation results of the reflector. The dashed lines represent the ideal delay time $\tau_{m,d}$. (a1)–(c1) received signal $y_{km}(t)$ from each transmitted element; (a2)–(c2) received signals $y_m(t)$; (a1)–(a3) results for $x = 0$ mm; (b1)–(b3) results for $x = -2.8$ mm; (c1)–(c3) results for $x = -4.8$ mm.

$$\theta_{mML} = \sin^{-1}\left(\frac{c_{ML}}{c_w} \cdot \frac{x_m - x_{s_i}}{l_{s_im}}\right), \tag{12}$$

where c_{ML} is the speed of sound in the acoustic matching layer. By considering scattering, $y_{km}(t)$ transmitted from the kth element and received by the mth element is given by

$$y_{km}(t) = \sum_{s_i} y_{ks_im}(t). \tag{13}$$

By adding $\{y_{km}(t)\}$ to the transmitted elements $\{k\}$, the received signal at the mth received element $y_m(t)$ is obtained as follows:

$$y_m(t) = \sum_k y_{km}(t). \tag{14}$$

In the actual measurement, $y_m(t)$ is observed at the mth element and each component of $\{y_{km}(t)\}$ cannot be detected. However, by the simulation experiments in the present paper, $y_m(t)$ is decomposed into the element signals $\{y_{km}(t)\}$ of Eq. (13).

Alternatively in the present paper, we investigated $R(m; d)$ of Eq. (2) by clarifying the difference of $\{y_{km}(t)\}$ between the reflector and scatterer through the simulation experiments for each of the transmission aperture's widths ℓ_w (the number N_w of transmitting elements) of 19.2 (96 elements), 14.4 (72 elements), 9.6 (48 elements), 4.8 (24 elements), and 0.2 mm (1 element). The signal from a plate reflector was generated by adding all the signals received from point scatterers aligned densely at 20 μm intervals with a width of 50 mm. By aligning point scatterers at 20 μm intervals on a tilted line, the surface of the tilted reflector was simulated.

2.4. Water tank experiments

The ultrasound diagnostic equipment was ProSound SSD-α10 (Hitachi Aloka) with a sampling frequency of 40 MHz. A linear probe UST-5412 (center frequency: 7.5 MHz, number of elements: 192, and element pitch: 0.2 mm) was attached to the ultrasound diagnostic equipment. For transmission, each element was given a delay time so that the focal point was 30 mm, which simulated the depth from the skin surface to the thoracic spine. No apodization was applied for transmission and reception.

Figure 3 shows the water tank experimental system. The short axis of molybdenum wire with a diameter of 30 μm and the surface of an acrylic block were used as a scatterer and a reflector, respectively. The depths of both objects were 30 mm. The angular amplitude characteristics $\{R(m; d)\}$ acquired with changing the transmission aperture's widths $\{\ell_w\}$ were compared with the simulation results.

3. Results and discussion

3.1. Angular amplitude characteristics of scattering

First, we discuss the simulation results of angular amplitude characteristics $\{R_S(m; d)\}$ of scattering for a transmission aperture's width (ℓ_w) of 19.2 mm (96 transmitted elements). The received element number of $m = 47$ at the center position was set to $x = 0$ mm. Figures 4(a1) and 4(b1) show the received signals $y_{km}(t)|_{m=47}$ and $y_{km}(t)|_{m=23}$ at the received positions $x = 0$ and -4.8 mm, respectively, for each kth transmitted element. The dashed lines in these
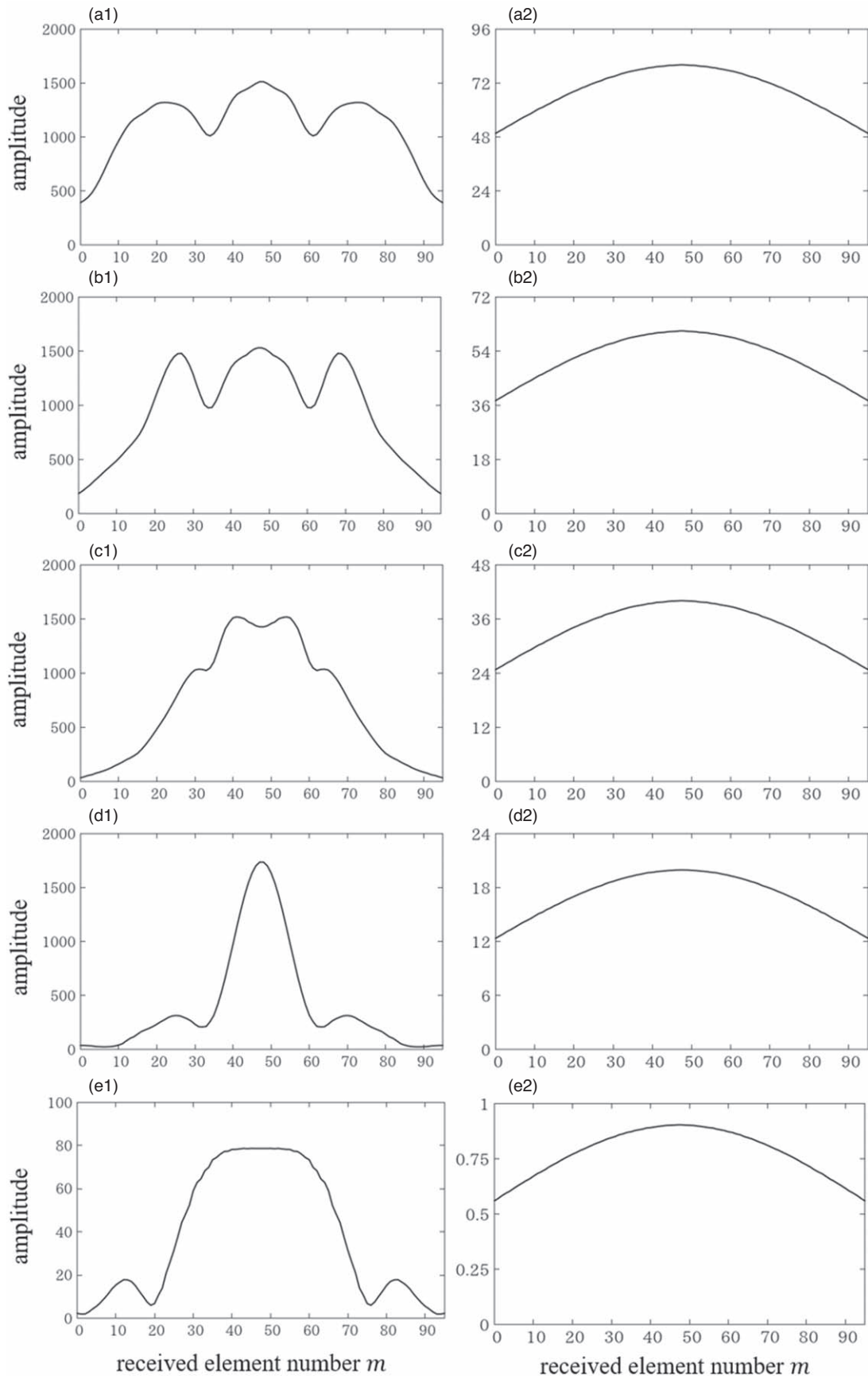
Fig. 6. Simulated angular amplitude characteristics of reflection and scattering for the different transmission aperture. (a1)–(e1) Reflection characteristics; (a2)–(e2) scattering characteristics; (a1), (a2) results for $\ell_w = 19.2$ mm; (b1), (b2) results for $\ell_w = 14.4$ mm; (c1), (c2) results for $\ell_w = 9.6$ mm; (d1), (d2) results for $\ell_w = 4.8$ mm; (e1), (e2) results for $\ell_w = 0.2$ mm.
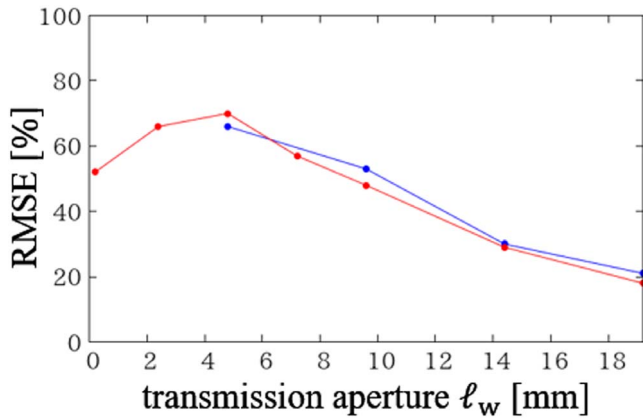
Fig. 7. (Color online) RMSE of the angular amplitude characteristics between reflection and scattering at different transmission aperture's widths $\{\ell_w\}$. Red dots show the results of the simulation experiment. Blue dots show the results of the water tank experiment.
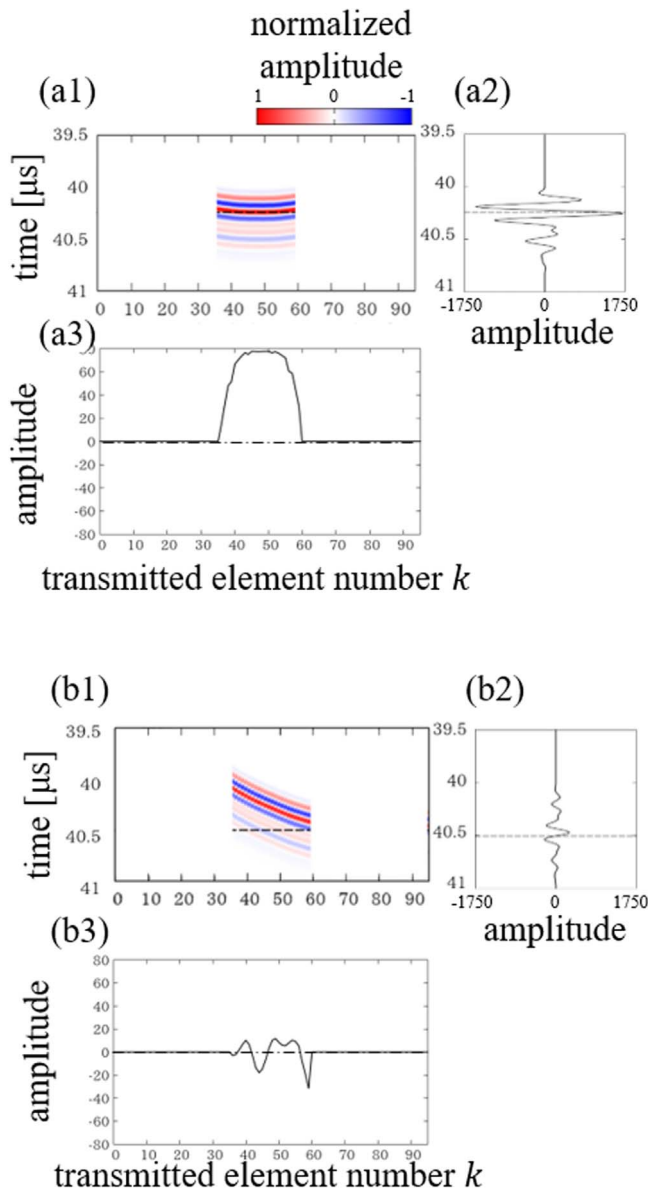

Fig. 8. (Color online) Simulation results of the reflector with a transmission aperture of 4.8 mm. The dashed lines represent the ideal delay time $\tau_{m,d}$. (a1), (b1) Received signal $y_{km}(t)$ from each transmitted element; (a2), (b2) received signals $y_m(t)$; (a1)–(a2) results for $x = 0$ mm; (b1), (b2) results for $x = -4.8$ mm.

figures show the ideal delay time $\{\tau_{m,d}\}$ calculated using Eq. (1). By integrating $\{y_{km}(t)|_{m=47}\}$ and $\{y_{km}(t)|_{m=23}\}$ along the direction of the transmitted elements $\{k\}$, Figs. 4(a2) and 4(b2) show the resultant waveforms of $y_m(t)|_{m=47}$ and $y_m(t)|_{m=23}$.

As shown in Figs. 4(a1) and 4(b1), $\{y_{km}(t)\}$ were received at the same time for each received element when the object was a scatterer and placed at the focal point. Thus, the shape of $y_m(t)$ was the same as that of the transmitted and received waveform $y_0(t)$ based on one element. When the received position m moved away from above the point scatterer, the signal amplitude in Fig. 4(b2) decreased owing to the receiving directivity of elements compared with that in Fig. 4(a2).

3.2. Angular amplitude characteristics of reflection
Next, we discuss the simulation results of angular amplitude characteristics $\{R_R(m; d)\}$ of reflection. Figures 5(a1), 5(b1), and 5(c1) show the received signals $\{y_{km}(t)|_{m=47}\}$, $\{y_{km}(t)|_{m=33}\}$, and $\{y_{km}(t)|_{m=23}\}$ at $x = 0$, -2.8, and -4.8 mm, respectively. Figures 5(a2), 5(b2), and 5(c2) show $y_m(t)|_{m=47}$, $y_m(t)|_{m=33}$, and $y_m(t)|_{m=23}$ at $x = 0$, -2.8, and -4.8 mm, respectively. Figures 5(a3), 5(b3), and 5(c3) show the amplitudes of the received signals $y_{km}(\tau_{m,d})|_{m=47}$, $y_{km}(\tau_{m,d})|_{m=33}$, and $y_{km}(\tau_{m,d})|_{m=23}$ at the ideal delay time $\tau_{m,d}$.

In Figs. 5(a1), 5(b1), and 5(c1), $\{y_{km}(t)\}$ was received earlier than the ideal delay time $\tau_{m,d}$ when the target was the reflector. This is because the propagation paths are shorter than those when the ultrasound is scattered at the focal point. Therefore, as shown in Figs. 5(a3), 5(b3), and 5(c3), $\{y_{km}(\tau_{m,d})\}$ are not constant for the transmitted elements k.

The following two things can be found in Fig. 5(a3). The first is that the angular amplitude characteristic $R_R(m = 47; d)$ at the central received element $m = 47$ has positively large amplitudes for 24 transmitted elements with $k = 36$–59. The second is that $R_R(m = 47; d)$ is negative for the transmitted elements around $k = 30$ and 65. By comparing Figs. 5(a3), 5(b3), and 5(c3), the profile of $\{y_{km}(\tau_{m,d})\}$ moved toward the transmitted elements on the right side. As a result of this movement, the negative components around $k = 65$ in Fig. 5(a3) were not received at $m = 23$, as shown in Fig. 5(c3).

3.3. Relationship between the width of the transmission aperture and angular amplitude characteristics
Figure 6 shows angular amplitude characteristics of reflection and scattering when the transmission aperture's width ℓ_w (the number N_w of transmitting elements) was 19.2 ($N_w = 96$), 14.4 ($N_w = 72$), 9.6 ($N_w = 48$), 4.8 ($N_w = 24$), and 0.2 mm ($N_w = 1$). The shape of $R_R(m)$ significantly changed as ℓ_w decreased, but the maximum value did not significantly change, except when $\ell_w = 0.2$ mm. On the other hand, the shape of $R_S(m)$ did not change, although its amplitude decreased in proportion to the decrease in ℓ_w.

This difference is caused by the fact that $\{y_{km}(\tau_{m,d})\}$ for the scattering were almost the same among the transmitted elements [Figs. 4(a1) and 4(b1)], whereas $\{y_{km}(\tau_{m,d})\}$ for the reflection significantly varied among the transmitted elements [Figs. 5(a3), 5(b3), and 5(c3)]. The decrease in ℓ_w corresponds to the exclusion of signals at both ends shown in Figs. 5(a3), 5(b3), and 5(c3).

For reflection, as the received element position (m) departed from the center, the shape of $\{y_{km}(\tau_{m,d})\}$ changed
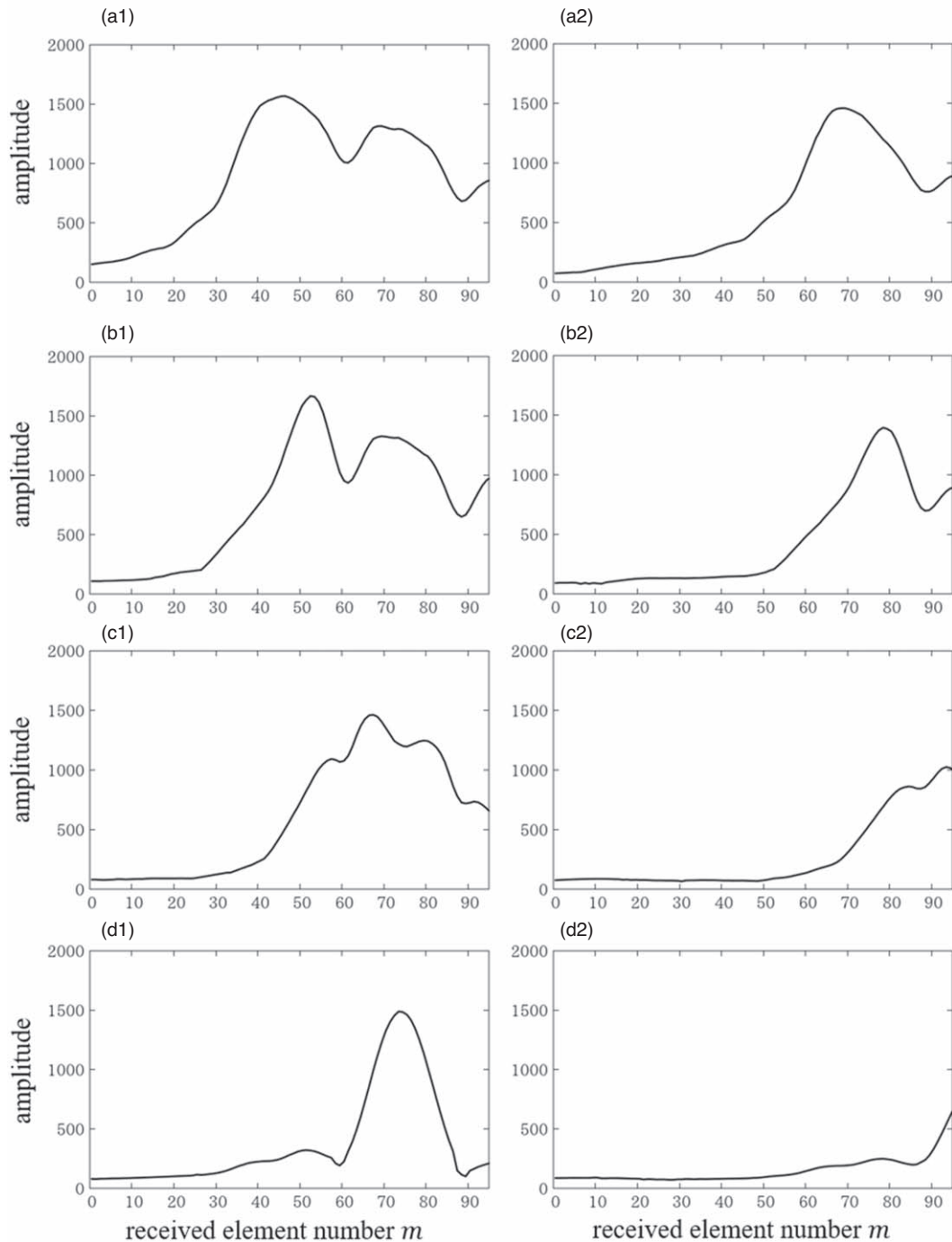
Fig. 9. Simulation results of angular amplitude characteristics of reflection for different transmission aperture's widths $\{\ell_w\}$. (a1)–(d1) Results for a reflector tilted by 5° with respect to the probe surface; (a2)–(d2) results for a reflector tilted by 10° with respect to the probe surface; (a1), (a2) results for $\ell_w = 19.2$ mm; (b1), (b2) results for $\ell_w = 14.4$ mm; (c1), (c2) results for $\ell_w = 9.6$ mm; (d1), (d2) results for $\ell_w = 4.8$ mm.

[Figs. 5(a3), 5(b3), and 5(c3)], and the transmitted elements $\{k\}$ with large amplitudes of $\{y_{km}(\tau_{m,d})\}$ shifted toward the end. Therefore, as ℓ_w decreased, $R_R(m)$ became small.

The RMSE between $\{R_R(m; d)\}$ and $\{R_S(m; d)\}$ for each transmission aperture's width (ℓ_w) is denoted with red dots in Fig. 7. The cases of $\ell_w = 2.4$ mm ($N_w = 12$) and $\ell_w = 7.2$ mm ($N_w = 36$) were also calculated and added. The case of $\ell_w = 4.8$ mm ($N_w = 24$) can emphasize the difference.

Figures 8(a1) and 8(b1) show the received signals $\{y_{km}(t)|_{m=47}\}$ and $\{y_{km}(t)|_{m=23}\}$ at $x = 0$ and 4.8 mm for each kth transmitted element, respectively, for $\ell_w = 4.8$ mm

($N_w = 24$). Figures 8(a2) and 8(b2) show the received signal $y_m(t)$ at $x = 0$ and -4.8 mm, respectively. Figures 8(a3) and 8(b3) show the amplitudes of the received signals $\{y_{km}(\tau_{m,d})|_{m=47}\}$ and $\{y_{km}(\tau_{m,d})|_{m=23}\}$ at the ideal delay times $\tau_{m,d}$, respectively.

The reason for the RMSE being maximized for $\ell_w = 4.8$ mm ($N_w = 24$) can be explained in two points: first, as shown in Fig. 8(a3), when ℓ_w was 4.8 mm (24 elements) or more, $R_R(47; d)$ was almost the same for $k = 36$–59, which accounted for a large fraction of $R_R(47; d)$ at the center with regard to the received element; second, as shown in
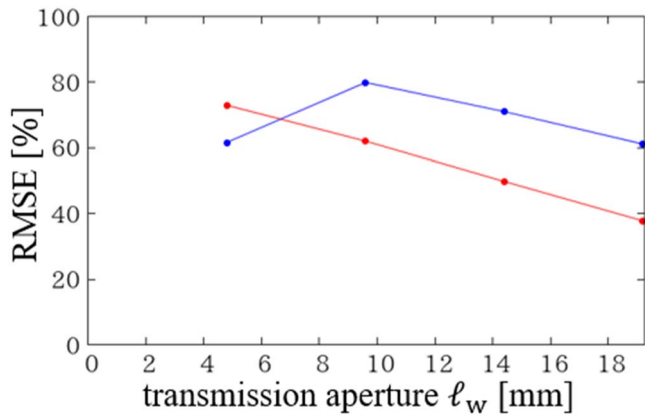
Fig. 10. (Color online) Simulation results of the RMSE of angular amplitude characteristics between reflection and scattering at different transmission aperture widths $\{\ell_w\}$. Red and blue dots show the results for a reflector tilted by 5° and 10°, respectively.

Figs. 5(a3), 5(b3), and 5(c3), the shape of $\{y_{km}(\tau_{m,d})\}$ changed as the received element position shifted. When $\ell_w = 4.8$ mm ($N_w = 24$), as shown in Fig. 8(b3), for the received element position (m) apart from the center, the received signal decreased with the change in $\{y_{km}(\tau_{m,d})\}$. When ℓ_w is larger than 4.8 mm, the number of transmitted elements with a large amplitude of $\{y_{km}(\tau_{m,d})\}$ does not decrease even if the shape of $y_{km}(\tau_{m,d})$ changes slightly; therefore, the width of the peak of $R_R(m; d)$ increases, and the RMSE with the angular amplitude characteristic of scattering $R_S(m; d)$ decreases. When ℓ_w is narrower than 4.8 mm, the peak of $R_R(m; d)$ decreases because all the signals from the transmitted elements of $k = 36–59$ have not been received. Therefore, the RMSE between $R_R(m; d)$ and $R_S(m; d)$ is maximum when $\ell_w = 4.8$ mm ($N_w = 24$).

Next, we investigated the case in which the reflector was inclined to the probe surface. Figure 9 shows the angular amplitude characteristics of reflection and scattering when the reflector was tilted by 5° or 10° concerning the probe surface. The signals with large amplitude were detected with the end of the received elements $\{m\}$ as the tilt angle increased. When the reflector was tilted by 10°, the amplitudes decreased with decreasing ℓ_w, because most of the reflected signals could not be received at the receiving elements; this was because of the tilt of the reflector.

The RMSEs between $\{R_R(m; d)\}$ and $\{R_S(m; d)\}$ for each transmission aperture's width (ℓ_w) when the reflector was tilted by 5° or 10° to the probe surface are denoted with red and blue dots, respectively in Fig. 10. When the reflector inclination was 5°, the RMSE was maximum for $\ell_w = 4.8$ mm ($N_w = 24$). The tendency was the same as the result for the parallel reflector in Fig. 7. When the reflector was tilted by 10°, the RMSE also increased with decreasing ℓ_w, although the RMSE for $\ell_w = 4.8$ mm was almost the same as that for $\ell_w = 19.2$ mm ($N_w = 96$). This is because most of

the reflected signals could not be received at the receiving elements for $\ell_w = 4.8$ mm. Therefore, it suggests that the bone surface should be aligned as parallel as possible to the probe surface in clinical applications.

In the simulation, the reflector was assumed to be flat; therefore, if the reflector was tilted to the probe surface in the elevational direction of the probe, the shape of $\{R_R(m; d)\}$ did not change. However, the angular amplitude characteristics from the curved surfaces such as the thoracic vertebrae would change due to phase aberration. We will investigate this effect further in our future work.

3.4. Results of the water tank experiment
Figure 11 shows $\{R_R(m; d)\}$ of reflection and $\{R_S(m; d)\}$ of scattering for each transmission aperture's width (ℓ_w); these were obtained from the surface of the acrylic block and the short axis of the wire, respectively, in the water tank experiment. The received signal was too weak while measuring the scatterer when $\ell_w = 0.2$ mm. The results were almost similar to Fig. 6. In Fig. 7, the blue dots show the RMSE between $\{R_R(m; d)\}$ and $\{R_S(m; d)\}$ for each value of ℓ_w. Reflectors and scatterers can be distinguished in detail when $\ell_w = 4.8$ mm.

3.5. Effect of the decreased transmission aperture's width on the lateral resolution
The reduction in ℓ_w affects the lateral resolution of the focused wave. Figure 12(a) shows the acoustic field distribution along the lateral direction x at a focal depth of 30 mm for each ℓ_w. The horizontal axis represents the lateral position centered just above the beam. The vertical axis was normalized to the maximum amplitude for each value of ℓ_w. The full-width-at-half-maximum (FWHM) increased as ℓ_w decreased.

Figure 12(b) shows the relationship between the FWHM of the transmitted beam at the focal depth and RMSE of $\{R_R(m; d)\}$ and $\{R_S(m; d)\}$. There is a trade-off between the lateral resolution and RMSE. In thoracic spine measurements in the clinic, it is necessary to determine the appropriate transmission aperture's width ℓ_w for imaging by considering this trade-off relationship.

4. Conclusions
We investigated the ultrasound transmission conditions so that differences in the angular amplitude characteristics of reflection and scattering are emphasized more. We discussed the angular amplitude characteristics $\{R_R(m; d)\}$ and $\{R_S(m; d)\}$ of the reflection and scattering based on the simulation and the water tank experiment and clarified the relationship between the angular amplitude characteristics and transmission aperture's width ℓ_w. For the measurement of the human thoracic vertebrae, it is necessary to consider the effect of the lateral resolution by changing ℓ_w and to investigate a suitable ℓ_w. The simulation and water tank experimental results showed that the difference between $\{R_R(m; d)\}$ and $\{R_S(m; d)\}$ is emphasized more, and it will significantly support thoracic epidural anesthesia in the future.
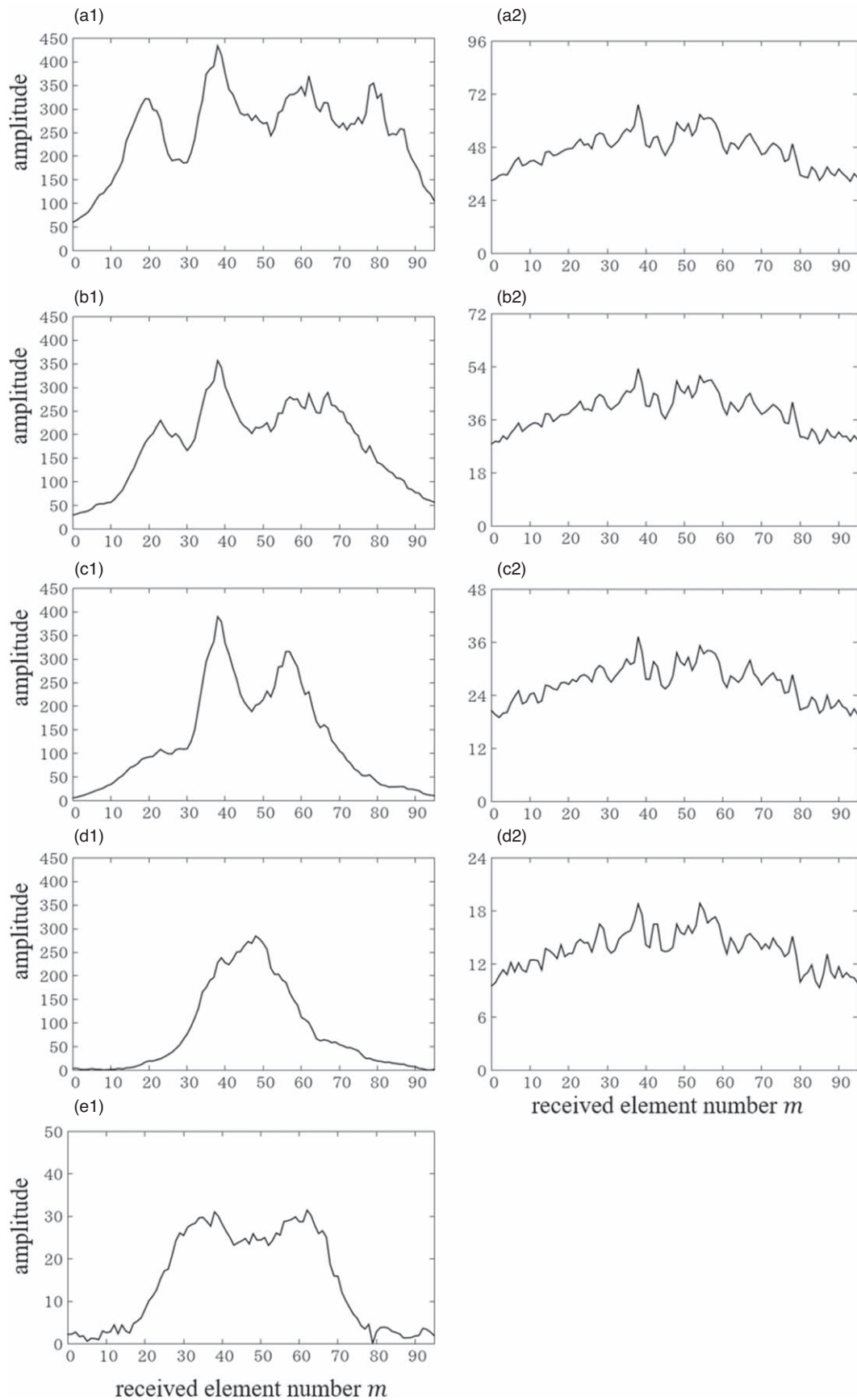
Fig. 11. Angular amplitude characteristics of reflection and scattering for the different transmission aperture $\{\ell_w\}$ obtained from the water tank experiment. (a1)–(e1) Reflection characteristics, (a2)–(e2) scattering characteristics, (a1), (a2) results for $\ell_w = 19.2$ mm; (b1), (b2) results for $\ell_w = 14.4$ mm; (c1), (c2) results for $\ell_w = 9.6$ mm; (d1), (d2) results for $\ell_w = 4.8$ mm, (e1) results for $\ell_w = 0.2$ mm. At $\ell_w = 0.2$ mm, signals of the scatterer were weak and could not be detected.
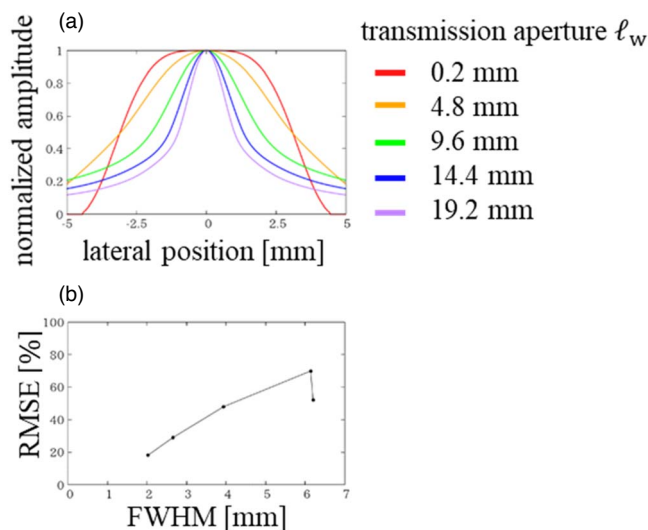
Fig. 12. (Color online) Relationship between the transmission aperture's width $\{\ell_w\}$ and the acoustic field distribution. (a) Acoustic field distribution along the lateral direction at a focal depth of 30 mm for each transmission aperture $\{\ell_w\}$. (b) Relationship between the FWHM of the transmitted beam and the RMSE of the angular amplitude characteristics of reflection and scattering at the focal depth.

Acknowledgments

1) R. D. Miller, L. I. Eriksson, J. P. Wiener-Kronish, N. H. Cohen, and W. L. Young, *Miller's Anesthesia* (Saunders, Amsterdam, 2015).
2) C. Konrad, G. Schupfer, M. Wietlisbach, and H. Gerber, Anesth. Analg. **86**, 635 (1998).
3) G. Le Coq, B. Le Ducot, and D. Benhamou, Can. J. Anaesth. **45**, 719 (1998).
4) M. P. Lewis, P. Thomas, L. F. Wilson, and R. C. Mulholland, Anesthesia **47**, 47 (1992).
5) B. Finucane, *Complications of Regional Anesthesia* (Springer, New York, 2009).
6) M. Yamauchi, Trends Anaesth. Crit. Care **2**, 234 (2012).
7) M. Nassar and I. A. Abdelazim, J. Clin. Monit. Comput. **29**, 573 (2015).
8) C. Alwin, Anesthesia **33**, 674 (2020).
9) B. Grosse, S. Eberbach, H. O. Pinnschmidt, D. Vincent, M. Schmidt-Niemann, and K. Reinshagen, BMC Anesthesiol. **20**, 256 (2020).
10) J. A. Lim, S. Y. Sung, J. H. Lee, S. Y. Lee, S. G. Kwak, T. Ryu, and W. S. Roh, Medicine **99**, e21684 (2020).
11) T. Grau, R. W. Leipold, S. Delorme, E. Martin, and J. Motsch, Reg. Anesth. Pain Med. **27**, 200 (2002).
12) M. Tiourririne, A. J. Dixon, F. W. Mauldin Jr, D. Scalzo, and A. Krishnarai, Invest. Radiol. **52**, 447 (2017).
13) H. Rafi-Tari, V. A. Lessowav, A. A. Kamani, P. Abolmaesumi, and R. Rohling, Ultrasound Med. Biol. **41**, 2220 (2015).
14) M. Pesteie, V. Lessowav, P. Abolmaesumi, and R. N. Rohling, IEEE Trans. Med. Imaging **37**, 81 (2018).
15) T. T. Oh, M. Ikhsan, K. K. Tan, S. Rehena, N. R. Han, A. T. H. Sia, and B. L. Sng, BMC Anesthesiol. **19**, 57 (2019).
16) N. Quader, A. Hodgson, and R. Abugharbieh, CLIP@MICCAI, 2014, p. 76.
17) F. Ozdemir, E. Ozkan, and O. Goksel, Conf. Proc. Medl Image Comput Asiist Interv., 2016, p. 256.
18) S. Yu, K. K. Tan, B. L. Sng, S. Li, and A. T. H. Sia, Proc. IEEE 12th Int. Symp. Biomed Imag, 2015, p. 243, 10.1109/ISBI.2015.7163859.
19) T. T. Y. Lee, W. W. Jiang, C. L. K. Cheng, K. K. L. Lai, M. K. T. To, R. M. Castelein, J. P. Y. Cheung, and Y. P. Zheng, Ultrasound Med. Biol. **45**, 2725 (2019).
20) Y. S. Wong, K. K. L. Lai, Y. P. Zheng, L. L. N. Wong, B. K. W. Ng, A. L. H. Hung, B. H. K. Yip, W. C. W. Chu, A. W. H. Ng, and Y. Qiu, Ultrasound Med. Biol. **45**, 2866 (2019).
21) S. F. Eby, P. Song, S. Chen, Q. Chen, J. F. Greenleaf, and K. N. An, J. Biomech. **46**, 2381 (2013).
22) M. A. Hussain, A. J. Hodgson, and R. Abugharbieh, Ultrasound Med. Biol. **43**, 648 (2017).
23) I. Hacihaliloglu, R. Abugharbieh, A. J. Hodgson, and R. N. Rohling, Ultrasound Med. Biol. **35**, 1475 (2009).
24) P. Pandey, N. Quader, K. Mulpuri, P. Guy, R. Garbi, and A. J. Hodgson, Epic Series Health Sci. **3**, 301 (2019).
25) K. Takahashi, H. Taki, E. Onishi, M. Yamauchi, and H. Kanai, J. Appl. Phys. **56**, 07JF01 (2017).
26) T. Sakamoto, H. Taki, and T. Sato, Acoust. Sci. Technol. **32**, 143 (2011).
27) S. Kidera, T. Sakamoto, and T. Sato, IEEE Trans. Geosci. Remote Sens. **48**, 1993 (2010).
28) H. Taki, S. Tanimura, T. Sakamoto, T. Shiina, and T. Sato, J. Med. Ultrasonics **48**, 51 (2015).
29) T. Yokoyama, S. Mori, M. Arakawa, E. Onishi, M. Yamauchi, and H. Kanai, J. Med. Ultrasonics **42**, 3 (2019).
30) T. Hashimoto, S. Mori, M. Arakawa, E. Onishi, M. Yamauchi, and H. Kanai, J. Appl. Phys. **60**, SDDE15 (2021).
31) T. Bando, S. Mori, M. Arakawa, E. Onishi, M. Yamauchi, and H. Kanai, Proc. Symp. Ultrason. Electr., 2021, Vol. 41.
32) T. Hashimoto, S. Mori, M. Arakawa, E. Onishi, M. Yamauchi, and H. Kanai, Proc. Autumn Mtg. Acoust. Soc. Jpn., 2020, p. 76.
33) Y. Hashimoto, N. Akashi, and J. Kushibiki, "Measurements of ultrasonic attenuation coefficients of water in VHF/UHF range," IEICE Tech. Rep. US97-50, 1997, [in Japanese].